

An active repeating fast radio burst in a magnetized eruption environment

Y. Li,^{1†} S. B. Zhang,^{1,2†} Y. P. Yang,^{3,1†} C. W. Tsai,⁴ X. Yang,^{1,5} C. J. Law,^{6,7}
 R. Anna-Thomas,^{8,9} X. L. Chen,⁴ K. J. Lee,^{10,4,11} Z. F. Tang,^{1,5} D. Xiao,¹
 H. Xu,⁴ X. L. Yang,¹² G. Chen,¹ Y. Feng,¹³ D. Z. Li,¹⁴ R. Mckinven,^{15,16}
 J. R. Niu,⁴ K. Shin,^{17,18} B. J. Wang,⁴ C. F. Zhang,^{10,4} Y. K. Zhang,⁴ D. J.
 Zhou,⁴ Y. H. Zhu,⁴ Z. G. Dai,¹⁹ C. M. Chang,^{1,5} J. J. Geng,¹ J. L. Han,⁴ L.
 Hu,²⁰ D. Li,⁴ R. Luo,²¹ C. H. Niu,⁴ D. D. Shi,¹ T. R. Sun,¹ X. F. Wu,^{1,5*}
 W. W. Zhu,^{4,22*} P. Jiang,^{4,23*} B. Zhang^{24,25*}

¹Purple Mountain Observatory, Chinese Academy of Sciences, Nanjing 210023, P. R. China

²CSIRO Space and Astronomy, Australia Telescope National Facility, PO Box 76, Epping,
 NSW 1710, Australia

³South-Western Institute For Astronomy Research, Yunnan University, Yunnan 650504,
 P. R. China

⁴National Astronomical Observatories, Chinese Academy of Sciences, Beijing 100101,
 P. R. China

⁵School of Astronomy and Space Sciences, University of Science and Technology of China,
 Hefei, 230026, P. R. China

⁶Cahill Center for Astronomy and Astrophysics, MC 249-17 California Institute of
 Technology, Pasadena CA 91125, USA

⁷Owens Valley Radio Observatory, California Institute of Technology, Big Pine CA 93513,
 USA

⁸West Virginia University, Department of Physics and Astronomy, P. O. Box 6315,
 Morgantown, WV, USA

⁹Center for Gravitational Waves and Cosmology, West Virginia University, Chestnut Ridge
 Research Building, Morgantown, WV, USA

¹⁰Department of Astronomy, Peking University, Beijing 100871, P. R. China

¹¹Kavli Institute for Astronomy and Astrophysics, Peking University, Beijing 100871,
 P. R. China

¹²Shanghai Astronomical Observatory, Chinese Academy of Sciences, Shanghai 200030,
 P. R. China

¹³Zhejiang Lab, Hangzhou, Zhejiang 311121, P. R. China

¹⁴Department of Astrophysical Sciences, Peyton Hall, Princeton University, Princeton, NJ

08544, USA

- ¹⁵Department of Physics, McGill University, 3600 rue University, Montréal, QC H3A 2T8, Canada
- ¹⁶Trottier Space Institute, McGill University, 3550 rue University, Montréal, QC H3A 2A7, Canada
- ¹⁷MIT Kavli Institute for Astrophysics and Space Research, Massachusetts Institute of Technology, 77 Massachusetts Ave, Cambridge, MA 02139, USA
- ¹⁸Department of Physics, Massachusetts Institute of Technology, 77 Massachusetts Ave, Cambridge, MA 02139, USA
- ¹⁹Department of Astronomy, University of Science and Technology of China, Hefei 230026, P. R. China
- ²⁰McWilliams Center for Cosmology, Department of Physics, Carnegie Mellon University, 5000 Forbes Ave, Pittsburgh, 15213, PA, USA
- ²¹Department of Astronomy, School of Physics and Materials Science, Guangzhou University, Guangzhou 510006, P. R. China
- ²²Institute for Frontiers in Astronomy and Astrophysics, Beijing Normal University, Beijing 102206, P. R. China
- ²³Guizhou Radio Astronomical Observatory, Guizhou University, Guiyang 550025, P. R. China
- ²⁴Nevada Center for Astrophysics, University of Nevada, Las Vegas, NV 89154, USA
- ²⁵Department of Physics and Astronomy, University of Nevada, Las Vegas, NV 89154, USA
- *To whom correspondence should be addressed; E-mail: xfwu@pmo.ac.cn (X.F.W.); zhuww@nao.cas.cn(W.W.Z.); pjiang@nao.cas.cn (P.J.); bing.zhang@unlv.edu(B.Z.)
- †These authors contributed equally to this work.

Fast radio bursts (FRBs) are millisecond-duration radio bursts with unidentified extra-galactic origin. Some FRBs exhibit mild magneto-ionic environmental variations, possibly attributed to plasma turbulence or geometric configuration variation in a binary system. Here we report an abrupt magneto-ionic environment variation of FRB 20220529, a repeating FRB from a disk galaxy at redshift 0.1839. Initially, its Faraday rotation measure (RM) was $21 \pm 96 \text{ rad m}^{-2}$ over 17 months. In December 2023, it jumped to $1976.9 \text{ rad m}^{-2}$, exceeding twenty times of the standard deviation of the previous RM variation, and returned to the typical values within two weeks. Such a drastic RM

variation suggests a dense magnetized clump moving across the line of sight, possibly due to coronal mass ejection associated with a stellar flare. It indicates that the FRB likely has a companion star that produced the stellar flare.

One sentence summary: An abrupt substantial variance in the Faraday rotation measure indicates an eruptive magneto-ionic environment surrounding a fast radio burst.

Introduction

Fast radio bursts (FRBs) are cosmological radio bursts with millisecond durations (*1–3*). Some repeat, while others apparently do not (*4, 5*). While their origin remains unknown, some clues have been obtained from the repeatability (*4*), the association of a nearby FRB with a Milky Way magnetar (a highly magnetized neutron star) (*6–8*), the periodicity observed in one of them (*9*), as well as the environmental properties of FRBs (*10, 11*).

The local magneto-ionic environment could be probed using the polarization properties of FRBs, such as the rotation measure (RM), the convolution of the electron density n_e and the magnetic field parallel to the line of sight B_{\parallel} , $\text{RM} \propto \int n_e(l)B_{\parallel}(l)dl$. The RM amplitude of FRBs spans from one to over one hundred thousand rad m^{-2} , and the variances are usually in a similar order of magnitude. These features are suggested to originate from plasma turbulence or the configuration of a companion star (*10, 12–15*).

FAST and Parkes observations

FRB 20220529 was discovered by the Canadian Hydrogen Intensity Mapping Experiment (CHIME) on 29 May 2022 and reported via the Virtual Observatory Event (VOEvent) service, with a dispersion measure (DM) of $246.3 \pm 0.4 \text{ pc cm}^{-3}$ and a Milky Way contribution of $\text{DM}_{\text{MW}} = 39.93 \text{ pc cm}^{-3}$ (*16, 17*). Triggered by the discovery, we proposed to observe it using the Five-

hundred-meter Aperture Spherical radio Telescope (FAST), with the 19-beam receiver covering a frequency range of 1000 – 1500 MHz (18). Two bursts were detected during our initial two-hour observation, which began at 23:09:10.131 UTC on 22 June 2022. Since then, we have conducted a continuous monitoring campaign of FRB 20220529 using FAST, as well as the ultra-wide-bandwidth low-frequency (UWL) receiver of the Parkes telescope, covering frequencies from 704 MHz to 4032 MHz (19). Up to 29 January 2024, 101 observations totaling 49.4 hours were conducted with FAST, while Parkes had completed 57 observations totaling 126.7 hours. In total, we detected 1148 bursts in FAST observations and 56 bursts in Parkes observations. Notably, FRB 20220529 continues to show burst detection in nearly all FAST observations, making it stand out as one of the longest-active FRBs among all repeaters, with an average burst rate of about 25 bursts per hour (20). At the end of August 2022 and March 2023, it experienced two most active periods, each lasting 1 – 2 months. The peak rate was 204 bursts per hour. The temporal evolution of the properties of FRB 20220529 is presented in Fig. 1.

Localization and host galaxy

During the active period of FRB 20220529 in 2023, we carried out observation with the Karl G. Jansky Very Large Array (VLA) using the *realfast* fast transient detection system (21). We observed FRB 20220529 three times at frequencies ranging from 1 to 2 GHz, 3 hours each. Besides the standard visibility data recorded with a 3 s sampling time, the data with a sampling time of 10 milliseconds were streamed to the *realfast* system to search for bursts. There are two bursts detected. One of them is too faint, and we do not use its information in this study. The position of the brighter burst in the International Celestial Reference Frame (ICRF, J2000) is localized to be right ascension $\alpha = 01^{\text{h}}16^{\text{m}}25.014^{\text{s}}$, declination $\delta = +20^{\circ}37'56.6''$, with a positional uncertainty (1σ) of $0.3''$ (20).

We searched for the host galaxy in the Dark Energy Spectroscopic Instrument (DESI) Legacy Imaging Surveys (Fig. 2A). There are four galaxies within 10 arcseconds of the burst position, and the burst position is localized within one of them. We calculated the chance coincidence probability P_{cc} of the galaxies, and the galaxy PSO J019.1046+20.6327 is most likely to be the host, with a $P_{cc} = 0.013$. The host galaxy is an extended source with a best-fitting model being an exponential galaxy and a half-light radius of $1.17'' \pm 0.02''$, indicating that it is very likely a disk galaxy. We performed optical spectral observation of the host galaxy with the 10.4m Gran Telescopio Canarias (GTC) telescope with its OSIRIS and R500R grism. The spectrum obtained is presented in Fig. 2B. $H\alpha$, $H\beta$, and $[O\text{ III}] \lambda\lambda 4959, 5007$ doublet are identified. The redshift of the host galaxy is identified as $z = 0.1839 \pm 0.0001$. After correction of the extinction from the Milky Way, the $H\alpha$ luminosity is $L_{H\alpha} = 2.4 \times 10^{40} \text{ erg s}^{-1}$, which indicates a star-formation rate of $\text{SFR} = 0.13 M_{\odot} \text{ yr}^{-1}$. We performed a spectral energy distribution (SED) fitting with the DESI g, r, i band, and WISE w1 and w2 band photometric results to estimate the stellar mass of the host galaxy. The stellar mass is estimated to be $(2.7 \pm 0.7) \times 10^9 M_{\odot}$, and the specific star formation rate (sSFR) is 0.05 Gyr^{-1} . The burst is $1.4'' \pm 0.2''$ offset from the center of the host galaxy, corresponding to $4.40 \pm 0.6 \text{ kpc}$. The cumulative light fraction, the fraction of the total brightness fainter than the FRB region and the total galaxy, is $0.13_{-0.09}^{+0.15}$, indicating that the FRB is in a median-to-faint region of the host. The host galaxy contribution to DM could be estimated as $\text{DM}_{\text{host}} = \text{DM} - \text{DM}_{\text{MW}} - \text{DM}_{\text{MW,halo}} - \text{DM}_{\text{IGM}}$, where $\text{DM}_{\text{IGM}} = fz$ represents the contribution from the inter-galactic medium. Considering the DM contributions of the Milky Way and its halo (30 pc cm^{-3}) (22), and a nominal range of $850 < f < 1000$ (23), one can infer DM_{host} to be $0 - 24 \text{ pc cm}^{-3}$, consistent with the relatively large offset and small light fraction of the source with respect to the host galaxy. The host galaxy and sub-galactic environment of FRB 20220529 are consistent with those observed for other repeating FRBs (24), and indicate a relatively quiet environment. The basic properties

of FRB 20220529 are summarized in Table 1.

Polarization and Rotation Measure

Before December 2023, the polarization analysis of FRB 20220529 revealed that most bright bursts have a high level of linear polarization, whose fractions are typically $> 90\%$. The RM varied between -300 rad m^{-2} and $+300 \text{ rad m}^{-2}$, with a median $\overline{\text{RM}} = 21.2 \text{ rad m}^{-2}$ and a root-mean-square (rms) value $\sigma_{\text{RM}} = 95.8 \text{ rad m}^{-2}$. FRB 20220529 showed RM reversals many times, regardless of whether or not the expected Milky Way contribution of $-35 \pm 9 \text{ rad m}^{-2}$ is taken into account (25). The RM seems to show two similar fluctuation patterns before MJD 60200 (13 September 2023). However, after MJD 60200, such a similarity is no longer observed. Longer monitoring time is needed to test whether the RM evolution is periodic. In general, the RM evolution during this period is also consistent with fluctuation from a turbulent environment near the FRB source. Calculating the structure function during this period and fitting it with the form of $D_{\text{RM}}(\tau) \propto \tau^\alpha$, we obtained $D_{\text{RM}}(\tau) \propto \tau^{0.16}$, implying that the index of the turbulence power spectrum is about $-(\alpha + 2) \sim -2.16$. Thus, the turbulent medium has a shallow spectrum in the inertial range. This result means that the variation is possibly dominated by small-scale RM density fluctuations (26), which could naturally arise in supersonic turbulence (27, 28). Albeit with a lower median value of RM, FRB 20220529 has an RM variation amplitude before December 2023 similar to that of FRB 20201124A (29), suggesting that these two FRBs may reside in a similar magneto-ionic environment. The RM reversal behavior of FRB 20220529 is also similar to FRB 190520B, even though it has a much smaller amplitude (14).

An abrupt and significant boost of the RM appeared in the end of 2023. Prior to this event, the last RM detection was recorded on 18 October 2023, at a value of $-139.9 \pm 94.4 \text{ rad m}^{-2}$. Two 20-minute FAST observations were conducted on 7 and 22 November 2023, but no FRB

was detected. On 14 December 2023, another 20-minute observation of FAST detected four bursts, two of which provided successful RM measurements of $1976.9 \pm 83.8 \text{ rad m}^{-2}$ and $1975.9 \pm 108.6 \text{ rad m}^{-2}$ (Table 2). Remarkably, within just 57 days, the RM value jumped from $-139.9 \pm 94.4 \text{ rad m}^{-2}$ to $1976.9 \pm 83.8 \text{ rad m}^{-2}$. We conducted a series of monitoring with FAST and Parkes at intervals of 1–5 days during the first 20 days following the discovery (20). The burst rate in FAST observations during this period ranged from 0 to 15 bursts per hour, which is similar to the normal low state of this source. During the “RM flare” phase, we obtained 17 bursts with RM measurements in 10 observations (Table 2, fig. S1 and fig. S2). The RM evolution is presented in Fig. 1F. It is shown that the RM decreased monotonously and dropped to the normal $(-300, 300) \text{ rad m}^{-2}$ on 28 December 2023, i.e., in 14 days. During the rapid return of the RM, a decrease of the linear polarization fraction was observed. Specifically, on 28 December 2023, the linear polarization fraction dropped to $28 \pm 6 \%$. Subsequently, the linear polarization fraction recovered to $87 \pm 26 \%$ on 29 January 2024, consistent with the nearly full linear polarization observed in the normal state of FRB 20220529. The significance of such an “RM flare” could be quantified by $\text{SNR}_{\text{RM}} = (\text{RM}_{\text{peak}} - \overline{\text{RM}})/\sigma_{\text{RM}} = 20.4$, where σ_{RM} is the rms of RM before December 2023. Even if we define the $\overline{\text{RM}}$ and σ_{RM} with all the data, the significance is still as large as 7.8 (fig. S4). This is much more significant than RM variations of all other active repeaters (20). The relative variance to the median RM is $\Delta\text{RM}/\overline{\text{RM}} \sim 99.8$ and a relative variance rate of $\Delta\text{RM}/\overline{\text{RM}}/\Delta t \sim 1.75 \text{ day}^{-1}$. Such an abrupt variance is unprecedented and cannot be attributed to the plasma density fluctuations, nor evolution due to binary orbital motion.

Implications of the “RM flare”

The significant “RM flare” in a month-timescale suggests the emergence and disappearance of a magnetized blob along the line of sight. The length scale l of such an “object” that produced the

observed abrupt order-of-magnitude RM variation could be estimated with an assumed velocity v and the observed recovering timescale t , i.e., $l \sim vt \simeq 0.6 \text{ AU}(v/100 \text{ km s}^{-1})(t/10 \text{ day})$. The velocity may range from $\sim 10 \text{ km s}^{-1}$ (relative velocity of stars) to the speed of light c (relativistic ejecta from catastrophic events). Correspondingly, the length scale could be estimated as $l \sim (0.06 - 1700) \text{ AU}$, which corresponds to the size of a stellar system or a binary system. Other scenarios, such as a young supernova remnant surrounding the FRB source, predict a much longer timescale and are therefore disfavored (supplementary text).

Thus, the observed abrupt order-of-magnitude RM variation in the "RM flare" state should be generated by ejecta from the FRB source itself or a nearby object. Let us consider a magnetar engine as the source of FRB 20220529, as suggested by the smoking-gun evidence of a magnetar engine for the Galactic FRB 20200428D (7, 8, 30, 31). The magnetized blob that is responsible for the abrupt RM variation would be a result of an outflow from the magnetar or from a companion star nearby. Various arguments, both observational and theoretical, are against the magnetar itself as the origin of the "RM flare". First, observationally, hundreds of X-ray bursts were detected during the explosion period of FRB 20200428D. A large number of magnetar outflows should be launched, but no significant RM variation was observed from the source (6, 32). Second, if an "RM flare" state is related to a high FRB burst rate (33–35), one should see a correlation between RM and burst rate. However, we notice that the burst rate in the "RM flare" state is normal and even slightly lower than that in the low RM state (as shown in Fig. 1). Finally, theoretically a magnetar outflow is believed to be mainly composed of relativistic electron-positron pairs. Such ejecta provide a very small RM contribution, as the Faraday rotation effects caused by the two particle species tend to cancel each other out, resulting in relativistic pairs having a nearly zero RM contribution (26). The same can be said for the continuous magnetar wind which is believed to be composed of pairs also. For all these reasons, we exclude the possibility that the magnetic blob that is responsible for the "RM flare"

originates from the FRB engine itself.

This leaves the only option that the “RM flare” is caused by a nearby object. The most likely scenario is that it originates from a coronal mass ejection (CME) associated with a stellar flare. The RM variation can be modeled by considering the expansion and passing through the line of sight of the CME (supplementary text). The sudden rise of RM corresponds to when the CME enters the line of sight, and the decay of RM can be attributed to the expansion of the plasma (which would reduce the number density and magnetic field in the blob) and its exit from the line of sight. One can study two detailed geometric models to fit the data (supplementary text): Case I includes both entrance and exit of the CME from the line of sight, and Case II attributes the decrease of RM only due to expansion with the CME never exiting the line of sight. The best-fit models are presented in Fig. 3 for the two cases. We can see that the observed RM evolution prefers the former scenario. According to this model, even if the CME contributes to a large RM, the DM contributed by the CME is estimated to be $\lesssim 1 \text{ pc cm}^{-3}$, which is consistent with the undetectable variation of DM during the “RM flare” phase. Since the probability of a CME moving across the line of sight is extremely low for an isolated FRB source, this model requires a companion star to eject the CME. Therefore, this observation gives a strong evidence that the FRB source is located in a binary system (36, 37).

Based on this event, one may predict that similar abrupt, significant RM variations can occur again in FRB 20220529 and probably other repeating FRB sources as well. Even though stellar flares may be common for certain low-mass stars with strong convection near the surface (e.g., 10 flares per day per source) (38, 39), the detection rate of such “RM flares” is likely low because only line-of-sight CMEs can cause a significant observational signature. Because the physical parameters (e.g., explosion energy, CME mass, etc.) of the stellar flares have wide distributions (40–42), the maximum RM and the duration of similar events should have a lognormal distribution. Future observations can test such a prediction.

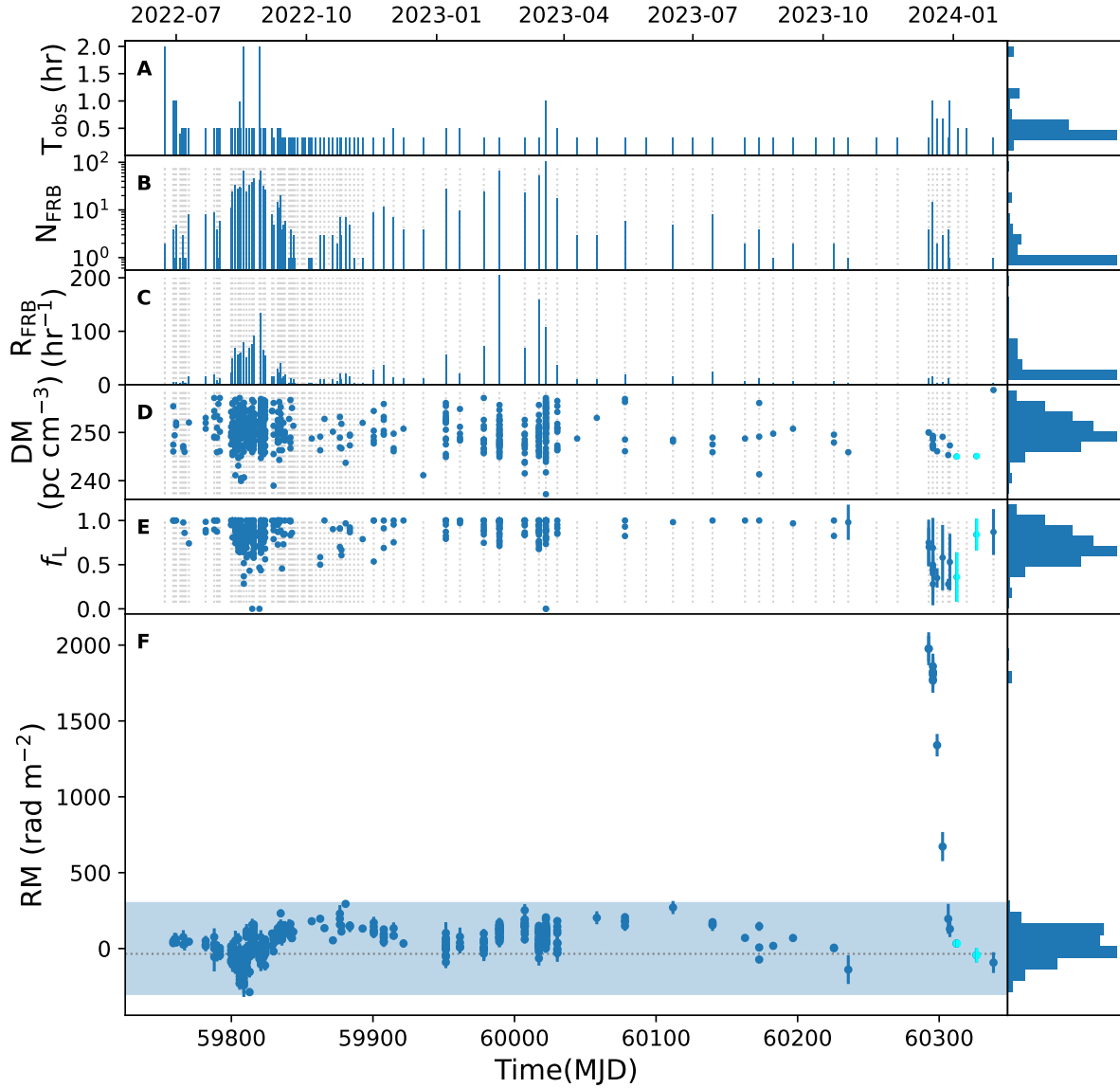


Figure 1: **Temporal variations of various quantities of FRB 20220529.** (A) Daily observing time. (B) Daily number of bursts detected. (C) Daily burst rate of FRBs. Vertical grey dotted lines present the days with observations, including days with non-detection. (D) Dispersion measure of all bursts. Blue dots are the bursts detected with FAST and cyan dots are those detected with Parkes. (E) Linear Polarization fraction of all bursts. (F) The Rotation measure and its evolution. The horizontal dotted line indicates the contribution of the Milky Way. The filled blue region indicates the range of the low RM state. A distinct RM flare is clearly seen.

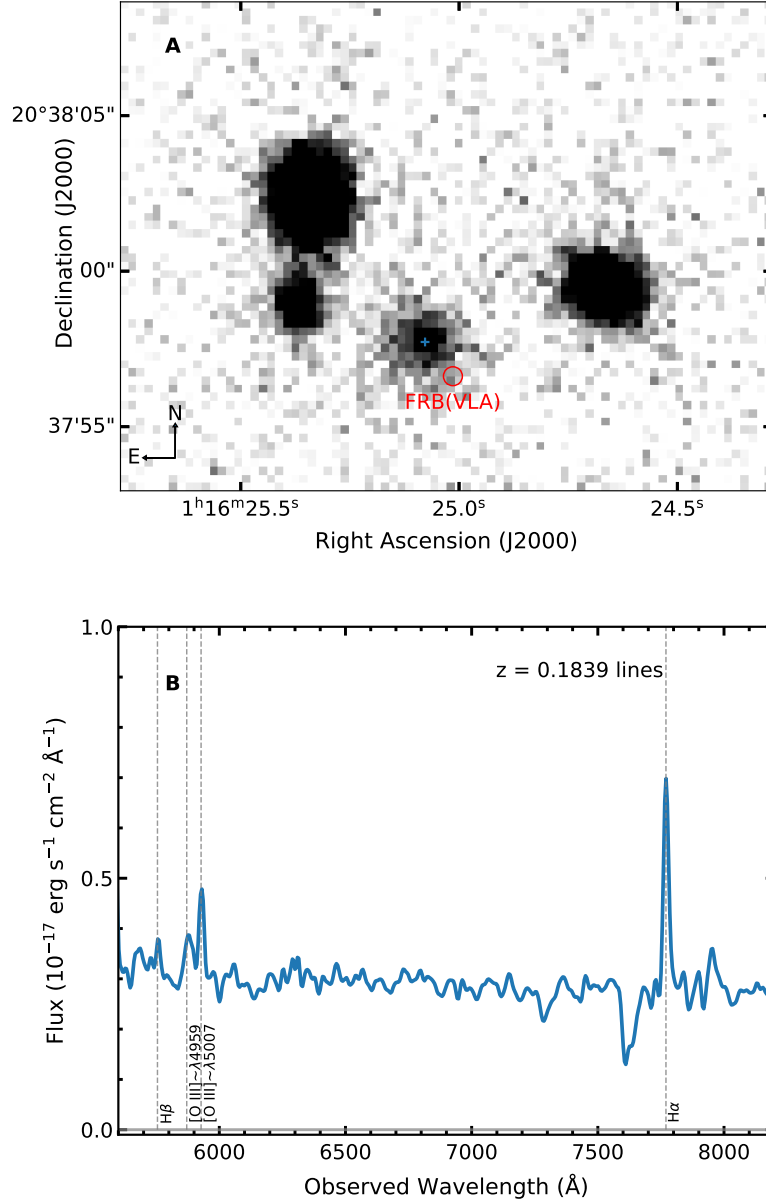


Figure 2: **Host-galaxy properties of FRB 20220529.** (A) DESI r -band image of the host galaxy of FRB 20220529. The FRB position from the VLA observation is overplotted as a red circle, and the center of the host galaxy is labeled as a blue cross. (B) GTC/OSIRIS spectrum of the FRB 20220529 host galaxy (blue). Emission lines from the $z = 0.1839$ host galaxy are labeled with gray dashed lines.

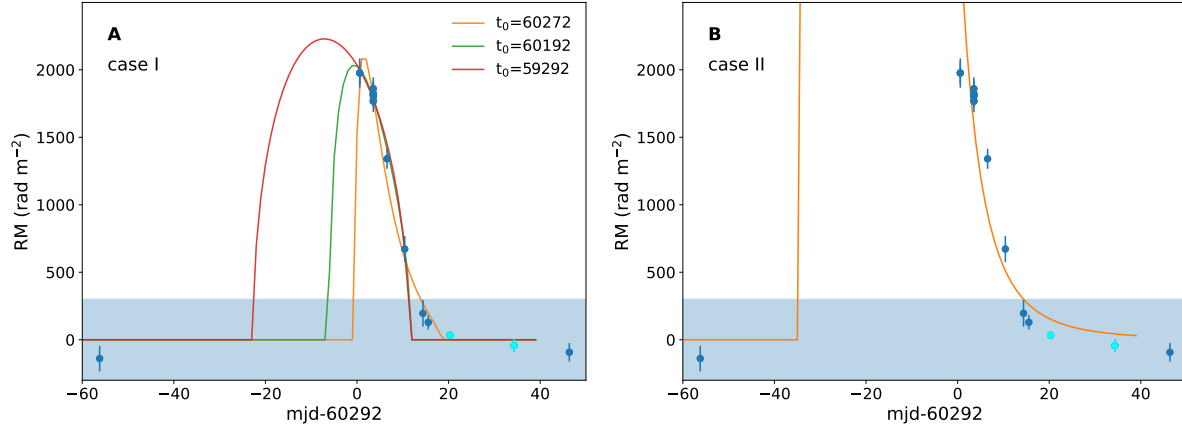


Figure 3: Fitting results for the stellar flare models. Blue dots are observed RM values from FAST, and cyan dots are from Parkes. **(A)** The best fits for Case I. The orange, green, and red lines correspond to assuming t_0 to be MJD = 60272, 60192, and 59292, respectively. **(B)** The best fit for Case II.

Table 1: **Basic Properties of FRB 20220529** All errors represent the 1σ uncertainties.

Burst Parameters:	
Right ascension (J2000)	$01^{\text{h}}16^{\text{m}}25.014^{\text{s}}$
Declination (J2000)	$+20^{\circ}37'56.6''$
positional uncertainty (")	0.3
Galactic coordinates (l, b)	(130.78767, -41.85802)
DM (pc cm^{-3})	250.2 ± 3.3
DM _{MW,NE2001} (16), DM _{MW,YMW16} (17) (pc cm^{-3})	39.95, 30.92
DM _{MW,halo} (pc cm^{-3})	30
DM _{host} [*] (pc cm^{-3})	0 – 24
RM _{MW} (rad m^{-2})	-35 ± 9
Host Galaxy:	
Redshift (z)	0.1839 ± 0.0001
Half-light radius (kpc)	3.60 ± 0.08
Offset (kpc)	4.4 ± 0.6
Normalized offset	1.2 ± 0.2
Probability of chance coincidence	0.013
Cumulative light fraction	$0.13^{+0.15}_{-0.09}$
Stellar mass (M_{\odot})	$(2.7 \pm 0.7) \times 10^9$
Star-formation rate ($M_{\odot} \text{ yr}^{-1}$)	0.13

* DM_{host} = DM – DM_{MW} – DM_{MW,halo} – fz and $850 < f < 1000$ is assumed.

Table 2: **Properties of FRB 20220529 bursts with RM measurements during the “RM flare” phase.** All errors represent the 1σ uncertainties.

MJD ^a	DM pc cm ⁻³	RM rad m ⁻²	f_L^b %
60235.7927564	245.9 ± 0.2	-139.9 ± 94.4	98 ± 20
60292.5811430	250.0 ± 0.4	1976.9 ± 83.8	75 ± 26
60292.5811432	250.0 ± 0.2	1975.9 ± 108.6	70 ± 22
60295.5377214	248.5 ± 0.3	1815.6 ± 44.6	40 ± 17
60295.5396355	246.7 ± 0.2	1825.1 ± 83.9	43 ± 19
60295.5440419	247.5 ± 0.3	1773.3 ± 30.6	69 ± 34
60295.5535219	249.3 ± 0.2	1860.1 ± 83.3	28 ± 24
60295.5587887	247.3 ± 0.2	1766.1 ± 44.0	50 ± 19
60295.5606052	247.1 ± 0.2	1815.5 ± 78.3	48 ± 13
60295.5625614	248.9 ± 0.3	1803.5 ± 117.4	45 ± 30
60298.5465724	246.1 ± 0.3	1340.3 ± 74.1	35 ± 11
60302.4196357	249.1 ± 0.5	671.9 ± 96.1	58 ± 37
60306.3962105	245.3 ± 0.2	195.7 ± 98.6	28 ± 6
60307.5594708	247.3 ± 0.8	128.8 ± 53.3	53 ± 32
60312.3030815 ^c	245.0 ± 0.4	33.0 ± 25.1	36 ± 28
60326.3185239 ^c	245.1 ± 0.5	-43.1 ± 47.5	84 ± 18
60338.3648098	258.8 ± 0.9	-92.8 ± 68.3	87 ± 26

^a MJDs are in barycentric dynamical time (TDB) and are referenced to infinite frequency.

^b Percentage of unbiased linear polarization along with 1σ uncertainty.

^c Bursts observed by Parkes.

References

1. D. R. Lorimer, M. Bailes, M. A. McLaughlin, D. J. Narkevic, F. Crawford, *Science* **318**, 777 (2007).
2. E. Petroff, J. W. T. Hessels, D. R. Lorimer, *Astron. Astrophys. Rev.* **27**, 4 (2019).
3. J. M. Cordes, S. Chatterjee, *Annu. Rev. Astron. Astrophys.* **57**, 417 (2019).
4. L. G. Spitler, *et al.*, *Nature* **531**, 202 (2016).
5. CHIME/FRB Collaboration, *et al.*, *Astrophys. J.* **257**, 59 (2021).
6. CHIME/FRB Collaboration, *et al.*, *Nature* **587**, 54 (2020).
7. C. D. Bochenek, *et al.*, *Nature* **587**, 59 (2020).
8. C. K. Li, *et al.*, *Nature Astronomy* **5**, 378 (2021).
9. CHIME/FRB Collaboration, *et al.*, *Nature* **582**, 351 (2020).
10. D. Michilli, *et al.*, *Nature* **553**, 182 (2018).
11. B. Marcote, *et al.*, *Nature* **577**, 190 (2020).
12. R. Luo, *et al.*, *Nature* **586**, 693 (2020).
13. G. H. Hilmarsson, *et al.*, *Astrophys. J.* **908**, L10 (2021).
14. R. Anna-Thomas, *et al.*, *Science* **380**, 599 (2023).
15. R. Mckinven, *et al.*, *Astrophys. J.* **950**, 12 (2023).
16. J. M. Cordes, T. J. W. Lazio, NE2001.I. A New Model for the Galactic Distribution of Free Electrons and its Fluctuations. arXiv:0207156 [astro-ph] (2002).

17. J. M. Yao, R. N. Manchester, N. Wang, *Astrophys. J.* **835**, 29 (2017).
18. P. Jiang, *et al.*, *Rev. Astron. Astrophys.* **20**, 064 (2020).
19. G. Hobbs, *et al.*, *Publ. Astron. Soc. Australia* **37**, e012 (2020).
20. Materials and methods are available as supplementary materials.
21. C. J. Law, *et al.*, *Astrophys. J.* **236**, 8 (2018).
22. K. Dolag, B. M. Gaensler, A. M. Beck, M. C. Beck, *Mon. Not. R. Astron. Soc.* **451**, 4277 (2015).
23. W. Deng, B. Zhang, *Astrophys. J.* **783**, L35 (2014).
24. S. Bhandari, *et al.*, *Astron. J.* **163**, 69 (2022).
25. N. Oppermann, *et al.*, *Astron. & Astrophys.* **575**, A118 (2015).
26. Y.-P. Yang, S. Xu, B. Zhang, *Mon. Not. R. Astro. Soc.* **520**, 2039 (2023).
27. P. Hennebelle, E. Falgarone, *Astronomy and Astrophysics Reviews* **20**, 55 (2012).
28. S. Xu, B. Zhang, *Astrophys. J.* **846**, L28 (2017).
29. H. Xu, *et al.*, *Nature* **609**, 685 (2022).
30. CHIME/FRB Collaboration, *et al.*, *Nature* **587**, 54 (2020).
31. S. Mereghetti, *et al.*, *Astrophys. J.* **898**, L29 (2020).
32. W. Zhu, *et al.*, *Science Advances* **9**, eadf6198 (2023).
33. B. D. Metzger, B. Margalit, L. Sironi, *Mon. Not. R. Astron. Soc.* **485**, 4091 (2019).

34. W. Lu, P. Kumar, B. Zhang, *Mon. Not. R. Astro. Soc.* **498**, 1397 (2020).
35. Y.-P. Yang, B. Zhang, *Astrophys. J.* **919**, 89 (2021).
36. K. Ioka, B. Zhang, *Astrophys. J.* **893**, L26 (2020).
37. F. Y. Wang, G. Q. Zhang, Z. G. Dai, K. S. Cheng, *Nature Communications* **13**, 4382 (2022).
38. R. A. Osten, S. J. Wolk, *Astrophys. J.* **809**, 79 (2015).
39. J. R. A. Davenport, *Astrophys. J.* **829**, 23 (2016).
40. C. E. Parnell, P. E. Jupp, *Astrophys. J.* **529**, 554 (2000).
41. T. Shibayama, *et al.*, *Astrophys. J.* **209**, 5 (2013).
42. M. N. Günther, *et al.*, *Astron. J.* **159**, 60 (2020).
43. J. Hickish, *et al.*, *Journal of Astronomical Instrumentation* **5**, 1641001 (2016).
44. A. W. Hotan, W. van Straten, R. N. Manchester, *Publ. Astron. Soc. Australia* **21**, 302 (2004).
45. S. M. Ransom, New search techniques for binary pulsars, Ph.D. thesis, Harvard University, Massachusetts (2001).
46. E. Petroff, *et al.*, *Mon. Not. R. Astro. Soc.* **447**, 246 (2015).
47. P. Kumar, *et al.*, *Mon. Not. R. Astro. Soc.* **500**, 2525 (2021).
48. J. E. Everett, J. M. Weisberg, *Astrophys. J.* **553**, 341 (2001).
49. K. C. Chambers, *et al.*, The Pan-STARRS1 Surveys. arXiv:1612.05560 [astro-ph] (2016).
50. J. S. Bloom, S. R. Kulkarni, S. G. Djorgovski, *Astron. J.* **123**, 1111 (2002).

51. J. X. Prochaska, *et al.*, *Journal of Open Source Software* **5**, 2308 (2020).
52. J. X. Prochaska, *et al.*, pypeit/PypeIt: Release 1.0.0 (2020).
53. E. Bertin, S. Arnouts, *Astronomy and Astrophysics Supplement* **117**, 393 (1996).
54. E. Komatsu, *et al.*, *Astrophys. J.* **180**, 330 (2009).
55. S. Noll, *et al.*, *Astron. & Astrophys.* **507**, 1793 (2009).
56. E. F. Schlafly, D. P. Finkbeiner, *Astrophys. J.* **737**, 103 (2011).
57. G. Bruzual, S. Charlot, *Mon. Not. R. Astro. Soc.* **344**, 1000 (2003).
58. C. M. Casey, *Mon. Not. R. Astro. Soc.* **425**, 3094 (2012).
59. R. C. Kennicutt, N. J. Evans, *Annu. Rev. Astron. Astrophys.* **50**, 531 (2012).

Acknowledgements

We are grateful to Qiang Yuan and Jingjing Li for helpful discussions. This work made use of data from the FAST. FAST is a Chinese national mega-science facility, built and operated by the National Astronomical Observatories, Chinese Academy of Sciences. The Parkes radio telescope (Murriyang) is part of the Australia Telescope National Facility, which is funded by the Australian Government for operation as a National Facility managed by CSIRO. This study is partially based on data collected at Karl G. Jansky Very Large Array, operated by the National Radio Astronomy Observatory (NRAO). The National Radio Astronomy Observatory is a facility of the National Science Foundation operated under cooperative agreement by Associated Universities, Inc. We acknowledge the use of public data from the DESI Legacy Survey. We gratefully acknowledge the support and assistance provided by the staff of the Gran Telescopio Canarias (GTC).

Funding

This work is partially supported by the National Natural Science Foundation of China (Grant Nos. 12321003, 12041306, 12103089, 11988101, 12303042, 12203045, 12003028, 12041303, 12303015), the National SKA Program of China (2022SKA0130100, 2022SKA0130101, 2022SKA0120103, 2020SKA0120200), the Natural Science Foundation of Jiangsu Province (Grant No. BK20211000, BK20231106), International Partnership Program of Chinese Academy of Sciences for Grand Challenges (114332KYSB20210018), the CAS Project for Young Scientists in Basic Research (Grant No. YSBR-063), the CAS Organizational Scientific Research Platform for National Major Scientific and Technological Infrastructure: Cosmic Transients with FAST, the Youth Innovation Promotion Association (2023331).

Author Contributions

Y.L., S.-B.Z., X.-F.W., and B.Z. coordinated the observational campaign, co-supervised data analyses and interpretations, and led the paper writing. S.-B.Z. and X.Y. led the radio data analyses. Y.-P.Y. led the interpretations and the paper writing. W.-W.Z. and B.Z. coordinated the regular monitoring program through the FAST FRB Key Science Project. P.J. coordinated the prompt FAST observation during the "RM flare" state. C.L., Y.L., C.-W.T., R.A.-T., X.-L.Y., and R.L. conducted the VLA observation and data analysis. C.-W.T. led the GTC observation campaign, and X.-L.C., G.C., Y.L., T.-R.S., D.-D.S. and L.H. contributed to the GTC spectrum campaign and optical data analysis. K.-J.L. contributed to the localization of the source. C.-M.C., J.-R.N., Y.-K.Z., B.-J.W., D.-J.Z., Z.-F.T., Y.F., C.-F.Z., D.-Z.L., R.M., K.S., C.-H.N., W.-W.Z., Y.-H.Z., H.X., R.L. aided the radio data analysis. D.X., J.-L.H., J.-J.G., Z.-G.D. and D.L. helped with the data interpolation.

Competing Interests

The authors declare no competing financial interests.

Data and materials availability:

FAST observational data can be accessed through the FAST data center at <http://fast.bao.ac.cn>, while Parkes raw data are available via CSIRO's data archive at <https://data.csiro.au/>. VLA raw data are available via VLA data archive size at <https://data.nrao.edu/portal/>. The reduced GTC spectrum is available through <https://github.com/Astroyx/FRB20220529>. Due to the large data volume, interested users are encouraged to contact the corresponding author to arrange the data transfer.

For code relevant to the analysis of the VLA observations, see <https://github.com/realfastvla/rfpipe>. The publicly available packages CASA (<https://casaguides.nrao.edu>), Heimdall ([20](http://</p></div><div data-bbox=)

[//sourceforge.net/projects/heimdall-astro](https://sourceforge.net/projects/heimdall-astro)), **PRESTO** (<https://github.com/scottransom/presto>), and **PSRCHIVE** (<http://psrchive.sourceforge.net>) can be found on their respective websites.

Supplementary materials

Materials and Methods

Supplementary Text

Figs. S1 to S6

Tables S1 to S2

References (43-59)

Supplementary Materials for:

An active repeating fast radio burst in a magnetized eruption environment

Y. Li, S. B. Zhang, Y. P. Yang, C. W. Tsai, X. Yang, C. J. Law, R. Anna-Thomas, X. L. Chen, K. J. Lee, Z. F. Tang, D. Xiao, H. Xu, X. L. Yang, G. Chen, Y. Feng, D. Z. Li, R. Mckinven, J. R. Niu, K. Shin, B. J. Wang, C. F. Zhang, Y. K. Zhang, D. J. Zhou, Y. H. Zhu, Z. G. Dai, C. M. Chang, J. J. Geng, J. L. Han, L. Hu, D. Li, R. Luo, C. H. Niu, D. D. Shi, T. R. Sun, X. F. Wu, W. W. Zhu, P. Jiang, B. Zhang

To whom correspondence should be addressed; E-mail: xfwu@pmo.ac.cn (X.F.W.); zhuww@nao.cas.cn(W.W.Z.); pjiang@nao.cas.cn (P.J.); zhang@physics.unlv.edu(B.Z.)

This PDF file includes:

Materials and Methods

Supplementary Text

Figs. S1 to S6

Tables S1 to S2

References (43-59)

S1 Materials and Methods

S1.1 FAST & Parkes observations

A brief summary of the radio observations is given in Table S1.

S1.1.1 FAST observations

Our campaign began with two consecutive one-hour grid observations, which started from 23:09:10.131 UTC on 22 June 2022, using all beams of the 19-beam receiver of the 500 m-diameter FAST radio telescope. This was triggered by the CHIME VOEvent report of the repeating FRB 20220529. After detecting two bursts on different beams and providing a derived location ($\alpha = 01^{\text{h}}16^{\text{m}}23.35^{\text{s}}$, $\delta = +20^{\circ}37'34.7''$), subsequent observations only using the central beam. We performed another two grid observations on 14 and 17 August 2022, as well as an off-beam tracking observation on 28 August 2022, to refine the position. Multiple bursts were detected in up to 3 beams simultaneously, suggesting a refined location: $\alpha = 01^{\text{h}}16^{\text{m}}24.24^{\text{s}}$, $\delta = +20^{\circ}38'27.6''$). The observations from 23 August 2022 to 14 February 2023 were operated with this position, and the subsequent observation using the localization of our VLA detection (see details in the below section), i.e. $\alpha = 01^{\text{h}}16^{\text{m}}25.01^{\text{s}}$, $\delta = +20^{\circ}37'57''$. Until 29 January 2024, we conducted 101 observations of FRB 20220529, totaling 49.4 hours. Considering the grid observations, the on-source tracking of FRB 20220529 is 43.4 hours. The 19-beam receiver covers a frequency range of 1000–1500 MHz with 4096 channels. The dual linear polarization signals were 8-bit sampled and channelized (18) using the Reconfigurable Open Architecture Computing Hardware generation 2 (ROACH 2) (43) and stored in PSRFITS search mode format (44). The sample time is 49.153 μs . Prior to each observation, a 1K equivalent noise-switched calibration signal was recorded to calibrate the results. The observation duration, the number of detected FRBs and the FRB rate are presented in Fig. 1. The observations on 22 June 2022 and 28 August 2022 do not have FRB rate information since they were

off-beam. The FRB rates on 14 and 17 August 2022 were estimated based on the bursts in the first half hour, during which the beam was on the source.

S1.1.2 Parkes observations

FRB 20220529 was monitored by Parkes using the Ultra-Wideband Low (UWL) receiver from 27 June 2022 to 29 January 2024, totaling 126.7 hours of 57 observations. Our Parkes observation followed the pointing of the FAST campaign. The UWL system covers frequencies from 704 MHz to 4032 MHz (19). Our data were 2-bit sampled every 32 or 256 μs , in each of the 1 or 0.125 MHz wide frequency channels, respectively. Coherent de-dispersion at a DM of 247 pc cm^{-3} with only one polarization was conducted before 27 September 2022, whereas full Stokes information has been collected since then. A 2-minute noise diode signal was injected for polarization calibration before each tracking observation.

S1.2 Burst detection

Data collected from the FAST and Parkes radio telescopes were processed using two individual search pipelines based on two pulsar/FRB single pulse searching packages PRESTO (45) and HEIMDALL (46). We processed the full band data from FAST, but divided the Parkes UWL into a series of sub-bands ranging from 128 to 3328 MHz based on a tiered strategy (47). In both pipelines, data sets were dedispersed in a range of DM values from 200 to 300 pc cm^{-3} , with a step of 0.1 pc cm^{-3} . Single pulse candidates with signal-to-noise ratio (S/N) greater than 7 were recorded and visually inspected. In total, there were 1148 bursts detected in FAST observations. 1073 bursts were detected when the source was on beam. Thus, the average FRB rate is 25 bursts per hour. 56 bursts were detected in Parkes observations. A detailed analysis of all burst properties will be presented in a companion paper.

S1.3 Polarization properties

The dispersion measure (DM) for each burst from FRB 20220529 was derived by maximizing the S/N of its integrated pulse profile. The de-dispersed polarization data were calibrated using the PSRCHIVE software package (44) with correction for differential gain and phase between the receivers achieved through the injection of a noise diode signal before each observation. Rotation measures (RMs) for all bursts were measured using the RMFIT program, searching for a peak in the linearly polarized flux $L = \sqrt{Q^2 + U^2}$, within the range of RM range from -4000 to 4000 rad m^{-2} , with a step of 1 rad m^{-2} . RMFIT corrects for Faraday rotation for each trial RM, producing a total linear polarization profile and an RM spectrum. A Gaussian fit was then applied to determine the optimal RM along with its 1σ uncertainty.

To compute the polarization fraction of each burst, we de-rotated its profiles at its best-fitted RM. Polarized pulse profile was generated by averaging over the frequency dimension. Due to the presence of noise, linear polarization L tends to be overestimated. To obtain an unbiased estimate, we used L_{unbias} (48)

$$f(x) = \begin{cases} \sigma_I \sqrt{\frac{L}{\sigma_I} - 1} & \text{if } \frac{L}{\sigma_I} \geq 1.57 \\ 0 & \text{otherwise} \end{cases} \quad (\text{S1})$$

where σ_I represents the off-pulse standard deviation in Stokes I.

S1.4 RM Variation

The observed RM evolution of FRB 20220529 includes two stages: 1) The low RM state (Before December 2023, over 500 days), the RM ranges from -300 rad m^{-2} to $+300 \text{ rad m}^{-2}$. The median value is $\text{RM} = 21.2 \text{ rad m}^{-2}$ and the scatter is $\text{rms} = 95.8 \text{ rad m}^{-2}$. The observed DM is $\text{DM} = 250.2 \text{ pc cm}^{-3}$, with a scatter of 3.3 pc cm^{-3} . There are two active periods with peak burst rates larger than 100 hr^{-1} in this stage. 2) The ‘‘RM flare’’ state (the end of December 2023), the RM jumped to $1976.9 \pm 83.8 \text{ rad m}^{-2}$ and then displayed a continuous decline from

$1976.9 \pm 83.8 \text{ rad m}^{-2}$ to $< 300 \text{ rad m}^{-2}$ within two weeks. No burst was detected in two 20-minute observations during the 57 days before the burst with the highest RM, from MJD=60235 to 60292. The observed DM in the “RM flare” state is almost consistent with those in the low RM state. The burst rate in the “RM flare” state is lower than that in the active periods in the low RM state.

The RM in the low RM state displayed a random evolution, which seems to originate from the turbulent environment near the FRB source. We calculated the structure function, which shows the variability on different timescales, using the RM values in the low RM state (i.e. before 1 November 2023). The result is presented in fig. S3. The structure function is fitted with a power law function $D_{\text{RM}}(\tau) \propto \tau^\alpha$ with the best-fit $\alpha = 0.16$. It implies that the index of the turbulence power spectrum is about $-(\alpha + 2) \sim -2.16$. Thus, the turbulent medium has a shallow spectrum in the inertial ranges. This result suggests that the variation is dominated by small-scale RM density fluctuations, which could naturally arise in supersonic turbulence (26).

The RMs in the “RM flare” state are significantly larger than those in the low RM state. The significance can be quantified with $\text{SNR}_{\text{RM}} = (\text{RM}_{\text{peak}} - \overline{\text{RM}})/\sigma_{\text{RM}} = 20.4$, where σ_{RM} is the standard deviation of RM in the background low RM state. In fig. S4, we compare the significance of FRB 20220529 with other repeating FRBs with long-term RMs, including FRB 20121102 (13), 20180916 (15), 20190520 (14), and 20201124 (29). Since there is no “RM flare” reported in other FRBs, we estimate their mean RMs and RM standard deviations with all the RM values and denote them as $\overline{\text{RM}}_{\text{all}}$ and $\sigma_{\text{RM,all}}$. To be consistent, the mean RM and RM standard deviation of FRB 20220529 in fig. S4 is also calculated with all the RM values. It is obvious that the “RM flare” in FRB 20220529 is very significant, and the duration is short. To compare, the RM variations of other FRBs are consistent with fluctuations within 3σ values. Although FRB 180916B also exhibited an RM increase after a prolonged stochastic period (15), the amplitude is much smaller and the timescale is long.

S1.5 VLA observation and localization

During the active period between January 2023 and April 2023, we conducted VLA observations under the director’s discretionary time (DDT) project 23A-385 (PI: Ye Li). The FRB field was observed with three 3-hour observations, two on 2023-02-18 and one on 2023-02-24. The observations were in a frequency range of 1 – 2 GHz with 1024 channels. The VLA antennas were in the B array configuration, with a maximum baseline of 11.1 km. The nominal spatial resolution is 4.3 arcsec in 1.5 GHz ¹.

Besides the standard visibility data recorded with a 3 s sampling time, the data with a sampling time of 10 milliseconds were also streamed to the *realfast* search system to search for bursts from FRB 20220529 in our VLA observations (21). Two FRBs were detected with the *realfast* system during our nine-hour observation. The one detected on 2023-02-18 was too faint, and we do not take its information into account here. The second burst was detected on 2023-02-24 at 22:12:41.97 UTC. We make an image with the raw visibilities dedispersed at the real-time detected DM, 237.8 pc cm⁻³, using CASA 6.1.4.12. After converting the visibilities in the science data model (SDM) format to measurement set (MS) format using the CASA tasks `importasdm`, we calibrate it using the task `applycal` with the CASA calibration tables from the NRAO Archive for this observation. The quasar 3C48 is used as a flux and bandpass calibrator, and J0122+2502 is used as a phase and amplitude calibrator. The calibrated measurement set was imaged using the CASA task `tclean` and the burst was fitted as an elliptical Gaussian with task `imfit`. It turns out the S/N is 12.6 in 1.39 – 1.43 GHz. We identify the position using `imfit` as 01^h16^m25.0124^s, +20°37′56.8270″ with 0.11″ and 0.12″ uncertainties in RA and Dec, respectively.

The systematic position error was estimated by comparing the objects in the radio continuum

¹<https://science.nrao.edu/facilities/vla/docs/manuals/oss/performance/resolution>

images and the PanSTARRS-DR2 stack catalog (49)². We reduced the standard visibility data with CASA 6.1.4.12 and made images for each observation individually, 0.5 arcsec per pixel. The sources are extracted with PyBDSF³. We selected true bright, compact radio sources using the following criteria: 1) Objects with other sources 10'' nearby are excluded to avoid the side-lobes of very bright sources. 2) The signal-to-noise ratio (the ratio between the peak flux and the background root-mean-square) is required to be larger than 5. 3) The peak flux is required to be larger than 70% of the total flux. 4) The source can be fitted with a single Gaussian, i.e., *S_Code* is 'S'. There are 84 point radio sources without nearby objects detected in the observational session. The radio sources are then cross-matched with the PanSTARRS-DR2 catalog within a separation of 1''. The trials for larger separations reveal that the cross-matched pairs with separations larger than 1'' are dominated by chance coincidence. Due to the significantly higher noise in the edge of the VLA field of view, only objects within 0.2 degrees of the center of the field of view are taken into account. There are 23 pairs cross-matched. We visually checked the radio images to ensure they were unresolved point sources and the optical counterparts were real. The median RA and Dec offsets between VLA and PanSTARRS catalog are $-0.024''$ and $0.204''$), respectively, and the systematic position errors between the radio positions and PanSTARRS positions are $0.161''$ and $0.196''$. Thus, the final localization of FRB 20220529 is $RA = 01^{\text{h}}16^{\text{m}}25.014^{\text{s}}$, $Dec = +20^{\circ}37'56.6''$ with a positional error of $0.3''$, dominated by the systematic uncertainty.

S1.6 Optical image and host galaxy identification

We explore host galaxy candidates in the DESI Legacy Survey. The DESI *r*-band image of the host galaxy is presented as Fig. 2A. For objects within 5 arcminutes of FRB 20220529, we exclude stars with detected parallax in Gaia and then calculate the chance coincidence proba-

²<https://catalogs.mast.stsci.edu/panstarrs/>

³<https://pybdsf.readthedocs.io/en/latest/index.html>

bility P_{cc} with the half-light radius r_{50} and r band magnitudes in the catalog (50). It turns out that the galaxy PSO J019.1046+20.6327 has the lowest $P_{cc} = 0.013$, while there are three more galaxies having $P_{cc} < 0.1$. Their coordinates, r band magnitudes, the half-light radii, the separation between FRB 20220529 and the center of the galaxies, as well as the chance coincidence probabilities P_{cc} , are listed in table S2.

S1.7 GTC spectrum observation

We observed the host galaxy of FRB 20220529 using OSIRIS+ Long Slit Spectroscopy (LSS) on the GTC telescope under project ID: GTCMULTIPLE1A-23ACNT (PI: C. W. Tsai) on 18 August 2023. A slit width of $1''$ and the R500R grism covering from 4800 \AA to 10000 \AA is used in order to cover the possible redshift range of the host galaxy, up to redshift 0.5. The observations were conducted on a dark night with a seeing of $0.9''$. Three 800 s exposure observations were conducted. The data were bias-subtracted, flat-fielded, cleaned of cosmic rays, wavelength calibrated using comparison-lamp spectra, and combined with PyPeit (51, 52) under standard techniques. The standard star ROSS 640 is utilized for flux calibration.

The combined spectrum is presented in Fig. 2B. There are many emission lines identified, including $H\alpha$, $H\beta$, $[\text{O III}] \lambda\lambda 4959, 5007$ doublet. We fit the spectrum with a power law indicating the continuum and Gaussian functions indicating the emission lines. The central wavelengths of the emission lines are tied together and shifted for different redshifts. The median pixel size of our spectrum is 4.9 \AA . Thus, we include the wavelength uncertainties with the Orthogonal Distance Regression (ODR) method⁴. With these emission lines, the redshift of the host galaxy is identified as $z = 0.1839 \pm 0.0001$.

⁴<https://docs.scipy.org/doc/scipy/reference/odr.html>

S1.8 Host Galaxy Properties

Offset and F_{light} : We localize the center of the host galaxy with the r band image of DESI Legacy Survey image using SExtractor (53)⁵ as RA = 01^h16^m25.078^s, Dec = +20°37'57.72". The offset between the FRB and the host galaxy center is calculated as 1.4 ± 0.2 arcsec, corresponding to $R_{\text{off}} = 4.4 \pm 0.6$ kpc at redshift 0.1839 ± 0.0001 using a Lambda cold dark matter (Λ CDM) cosmological model with standard parameters (54). The half-light radius of the host galaxy is provided in the DESI Legacy Survey catalog, which is $1.17'' \pm 0.02''$, corresponding to 3.60 ± 0.08 kpc. The normalized offset is $r_{\text{off}} = R_{\text{off}}/R_{50} = 1.2 \pm 0.2$. The offset information of FRB 20220529 is quite typical in FRBs (24).

In order to explore the environment of the FRB, we also estimate the cumulative light fraction F_{light} , the fraction of the total brightness of the regions fainter than the FRB position to the total brightness of the host with the r -band DESI Legacy Survey image. Following Lyman et al. (2017), we get the region of the host galaxy from SExtractor and sort the brightness of the pixels. The brightness of the FRB region is estimated from the position and error of the FRB with the ds9 region. The fractional brightness of the regions fainter than the FRB 20220529 region to the total brightness of the host is then estimated to be $F_{\text{light}} = 0.13^{+0.15}_{-0.09}$. Although the F_{light} is small, the uncertainty is quite large. It is consistent with core-collapse supernovae and binary mergers.

Stellar Mass: We make a broadband Spectral Energy Distribution (SED) fitting to explore the stellar masses of the host galaxy. The Code Investigating GALaxy Emission (CIGALE (55))⁶ is utilized with the Galactic extinction corrected (56) g, r, z band model fluxes from DESI Legacy Survey and the W1, W2 magnitudes from Wide-Field Infrared Survey Explorer (WISE) telescope. During the SED fitting, the stellar population model from (BC03 (57)) with

⁵<https://astromatic.net/software/sextractor/>

⁶<https://cigale.lam.fr/>

the Salpeter model as the initial mass function is used. An e-folding `sfhdelayed` model with an initial SFR of 0.1 is assumed as the star formation history. The `dustatt_calzleit` dust attenuation model with the UV bump centroid to be 217.5 nm, as well as the `casey2012` dust emission model (58), are used. No AGN is added. The resulting stellar mass is $M_* = (2.7 \pm 0.7) \times 10^9 M_\odot$.

Star Formation Rate (SFR): We use the luminosity of H α line $L_{\text{H}\alpha}$ to estimate the star formation rate (SFR). Firstly, we made the Galactic extinction corrections with $R_V = 3.1$ and $E(B - V)_{\text{MW}} = 0.0706 \text{ mag}$ (56)⁷. Then, the GTC spectrum is fitted with a power law as the continuum and Gaussian functions as emission lines. The slit correction is estimated by the fraction between the light within the slit and the entire galaxy in the galaxy segmentation provided by SExtractor. After correction, the H α flux is $2.5 \times 10^{-16} \text{ erg s}^{-1} \text{ cm}^{-2}$, corresponding to $2.5 \times 10^{40} \text{ erg s}^{-1}$ at redshift 0.1839 ± 0.0001 . The SFR can be estimated with the H α (59) as $\text{SFR} = L_{\text{H}\alpha} / (10^{41.27} \text{ erg s}^{-1}) = 0.13 M_\odot \text{ yr}^{-1}$. The specific SFR is then 0.05 Gyr^{-1} , consistent with repeating FRBs (24) as well as supernovae and SGRBs.

S2 Supplementary text

S2.1 Implications of the ‘‘RM flare’’

The observed RM evolution in the ‘‘RM flare’’ state is significantly different from that in the low RM state. It displays a continuous decline from 2000 rad m^{-2} to 200 rad m^{-2} over two weeks. If the FRB source is a magnetar, the observed RM variation in the ‘‘RM flare’’ state is not likely contributed by the magnetar outflow or the magnetar wind based on the current observation evidence. See the main text for details. Besides, the observed RM variation in the ‘‘RM flare’’ state does not prefer a young supernova remnant (SNR) due to the following

⁷<https://irsa.ipac.caltech.edu/cgi-bin/bgTools/nph-bgExec>

reasons: 1) The RM variation from a young SNR should be monotonic if the magnetic geometry along the line of sight does not experience significant change. Such a prediction is inconsistent with the observed feature. 2) Considering that the magnetic fields in the SNR are turbulent, a random RM variation could be generated due to the relative motion between the SNR and the FRB source. Since the power spectrum of the turbulence fluctuations usually satisfies a power-law distribution, the corresponding RM variation is predicted to be continuous, which cannot produce the observed abrupt order-of-magnitude RM variation within a short period of time. 3) in the SNR scenario, a random rapid RM variation with a significant amplitude requires the SNR to be very young with an age of a few years (26). Such a young SNR would produce excessive host DM and significant DM variation, which are not observed in FRB 20220529. Therefore, in the following discussion, we consider that the observed RM variation in the “RM flare” state is attributed to a coronal mass ejection (CME) associated with a stellar flare from the companion star in a binary system.

The CME could be treated as a blob that expands during its propagation. We consider a two-dimensional toy model for simplicity. We assume that the blob has a mass of M , an expanding speed of c_s , a bulk-motion velocity of v , an initial size of l_0 , and an initial magnetic field of B_0 . The blob expanding velocity depends on its sound speed,

$$c_s \sim \left(\frac{kT}{m_p} \right)^{1/2} \simeq 10 \text{ km s}^{-1} T_4^{1/2}. \quad (\text{S2})$$

We notice that the expanding speed c_s may be much smaller than the bulk-motion velocity $v \sim (10^2 - 10^3) \text{ km s}^{-1}$ for a typical CME of a stellar flare. At the distance $r = vt$ from the companion, the blob size is estimated as

$$l \simeq l_0 + c_s t \simeq \frac{c_s}{v} r. \quad (\text{S3})$$

Since $c_s t \sim 8 \times 10^{10} \text{ cm } t_{\text{day}}$ is of the order of the stellar radius R_* for the observing timescale $t \sim$ a few days, one always has $c_s t \sim R_* > l_0$. Assuming that the electron number density n_e

and the magnetic field strength B are uniform within the CME plasma, one has

$$n_e(r) \simeq \frac{M}{\mu_m m_p (4\pi/3) l^3} \simeq \frac{3M}{4\pi \mu_m m_p r^3} \left(\frac{v}{c_s}\right)^3, \quad (\text{S4})$$

$$B(r) \simeq B_0 \left(\frac{l}{l_0}\right)^{-2} \simeq B_0 \left(\frac{v}{c_s}\right)^2 \left(\frac{r}{l_0}\right)^{-2}, \quad (\text{S5})$$

where $\mu_m = 1.2$ is the mean molecular weight for a solar composition.

We define the angle between the blob velocity and the line of sight (LOS) as θ and consider three scenarios. The schematic configurations are presented in fig. S5. Case I: the blob can enter and eventually exit the LOS. Case II: the moving direction is close to the LOS with $\sin \theta < c_s/v$, and the blob can enter but never exit the LOS eventually. Case III: the blob never enters the LOS, and the moving direction is far away from the LOS with $\sin \theta > c_s/v$. In Case III, the RM of FRBs remains unchanged. We will discuss the first two scenarios in detail in the following discussion.

Case I requires $v \sin \theta > c_s$. Meanwhile, at the distance $r_c = vt_c$ from the star, the blob center reaches the LOS, corresponding to the peak time of the observed RM flare. We define the transverse distance from the blob center to the LOS as x , as shown in fig. S5. One then has

$$x(t) = v|t - t_c| \sin \theta. \quad (\text{S6})$$

We define the RM rising time as t_i , when the blob enters the LOS, then one has $x(t_i) = l(t_i) = c_s t_i$ with $t_i < t_c$, leading to

$$t_i = \frac{vt_c \sin \theta}{v \sin \theta + c_s}. \quad (\text{S7})$$

We define the time when RM decreases to the pre-flare value as t_f . One has $x(t_f) = l(t_f) = c_s t_f$ with $t_f > t_c$, leading to

$$t_f = \frac{vt_c \sin \theta}{v \sin \theta - c_s}. \quad (\text{S8})$$

Therefore, the total duration of the RM flare is

$$\Delta t = t_f - t_i = \frac{2(v/c_s) \sin \theta}{(v/c_s)^2 \sin^2 \theta - 1} t_c. \quad (\text{S9})$$

The observed variation of RM depends on the properties of the CME along the line of sight,

$$\text{RM}(t) \sim \frac{e^3}{2\pi m_e^2 c^4} n_e B d, \quad (\text{S10})$$

where d is the LOS scale of the blob, which can be estimated as

$$d(t) = 2\sqrt{l(t)^2 - x(t)^2}, \quad \text{with } x(t) < l(t). \quad (\text{S11})$$

Therefore, the RM evolution during the flaring state satisfies

$$\text{RM}(t) \sim t^{-5} \left[t^2 - \frac{v^2 \sin^2 \theta}{c_s^2} (t - t_c)^2 \right]^{1/2} \quad (\text{S12})$$

for $x(t) < l(t)$. Otherwise, $\text{RM}(t) \sim 0$. The RM evolution is shown in fig. S6.

Next, we consider that the blob moving direction satisfies $v \sin \theta < c_s$ and the transverse distance from the blob center to the LOS as x_* at t_* , corresponding to Case II in fig. S5. At time t , the transverse distance from the blob center to the LOS satisfies

$$x(t) = x_* + v(t - t_*) \sin \theta. \quad (\text{S13})$$

For the late-time evolution shown in the observation of FRB 20220529, one approximately has $x(t) \simeq vt \sin \theta$. The line-of-sight scale of the blob is estimated as

$$d(t) = 2\sqrt{l(t)^2 - x(t)^2} \simeq 2t\sqrt{c_s^2 - v^2 \sin^2 \theta}. \quad (\text{S14})$$

Therefore, the RM evolution approximately satisfies

$$\text{RM}(t) \sim t^{-4}. \quad (\text{S15})$$

Such a scenario predicts that the RM variation in the high state follows a power-law decay.

Based on the above discussion, one can estimate the typical RM value from the CME associated with a stellar flare from the companion star. At the observed timescale, one has

$$\begin{aligned} \text{RM} &\sim \frac{e^3}{2\pi m_e^2 c^4} \frac{3f_{\text{geo}} M B_0 l_0^2}{4\pi \mu_m m_p} \left(\frac{v}{c_s}\right)^4 (vt)^{-4} \\ &\sim 2.7 \times 10^3 \text{ rad m}^{-2} f_{\text{geo}} M_{17} B_{0,0} l_{0,-1,\odot}^2 v_8^{-4} t_{\text{day}}^{-4} (v/c_s)_2^4, \end{aligned} \quad (\text{S16})$$

where f_{geo} is a geometric factor. For Case I, one has $f_{\text{geo}} \sim [1 - (v^2 \sin^2 \theta / c_s^2)(1 - t_c/t)^2]^{1/2}$. For Case II, one has $f_{\text{geo}} \sim 1$. We assume that the mass, initial magnetic field, and length scale of the stellar flare are $M \sim 10^{17}$ g, $B_0 \sim 1$ G and $l_0 \sim 10^{-2} R_\odot$, respectively. Therefore, a typical stellar flare could contribute to the observed RM flare. In order to keep the radio wave transparent, we also estimate the electron number density $n_e \sim 2 \times 10^7 \text{ cm}^{-3} \ll 10^{10} \text{ cm}^{-3}$ when the blob crosses the LOS. Thus, the blob is transparent to the GHz waves. At last, the DM contributed by the CME could be estimated by

$$\text{DM} \sim n_e l \simeq 0.5 \text{ pc cm}^{-3} M_{17} c_{s,6}^{-2} t_{\text{day}}^{-2}, \quad (\text{S17})$$

which is much smaller than the observed DM and is consistent with the non-detection of significant DM variation as observed.

We performed a Bayesian inference of the parameters using standard MCMC techniques for Case I with Eq.(S12). To fit the observed data, we correct the observational time with a zero point t_0 when the stellar flare just occurred near the stellar surface. The emcee⁸ software package was applied. Because the period when $\text{RM} < 300 \text{ rad m}^{-2}$ has a high RM fluctuation, which is likely due to a different mechanism, we only require the model-predicted RM to be smaller than 300 rad m^{-2} during that period of time. For Case I, the initial time t_0 is not well constrained. We thus fit the model with different assumed t_0 values. For each run, 30 independent chains of 50,000 samples are operated, and the first 25,000 samples are discarded.

⁸<https://emcee.readthedocs.io/en/stable/>

For the initial time t_0 of MJDs = 60272, 60192, 59292 (-20, -100, 1000 days before the first time we observe the abrupt RM variance), the time when the blob center reaches the LOS is $t_c = 26.0^{+0.2}_{-0.4}$, $102.0^{+0.7}_{-1.1}$, 994^{+4}_{-8} days, and the best fitting $v^2 \sin^2 \theta / c_s^2 = 9.5^{+1.4}_{-0.7}$, 132^{+29}_{-29} , 3405^{+2414}_{-1773} , Fig. 3A shows the best-fit RM evolution curves with these parameters.

We also applied the MCMC method to explore the goodness of the fit for the model of Case II with Eq.(S15). 32 independent chains of 5,000 samples were applied, and the first 2000 samples were discarded. The zero time point is -17.46 ± 0.17 days before MJD 60292, and the logarithmic normalization is 8.49 ± 0.01 . The best-fit RM evolution curve is presented in Fig. 3B. This model predicts a very high RM (as high as $60235 < \text{MJD} < 60292$) at the peak time, during which we did not detect any FRBs. Observations during the rising phase would have constrained the model parameters much better.

The linear polarization degree seems to show a delayed decrease along with the regression of the RM. It indicates that the plasma contributing to the RM does not directly cause depolarization. Alternatively, the properties of the plasma may change during the RM regression. However, the uncertainty of the linear polarization degree is too large, which prevents us from drawing a firm conclusion.

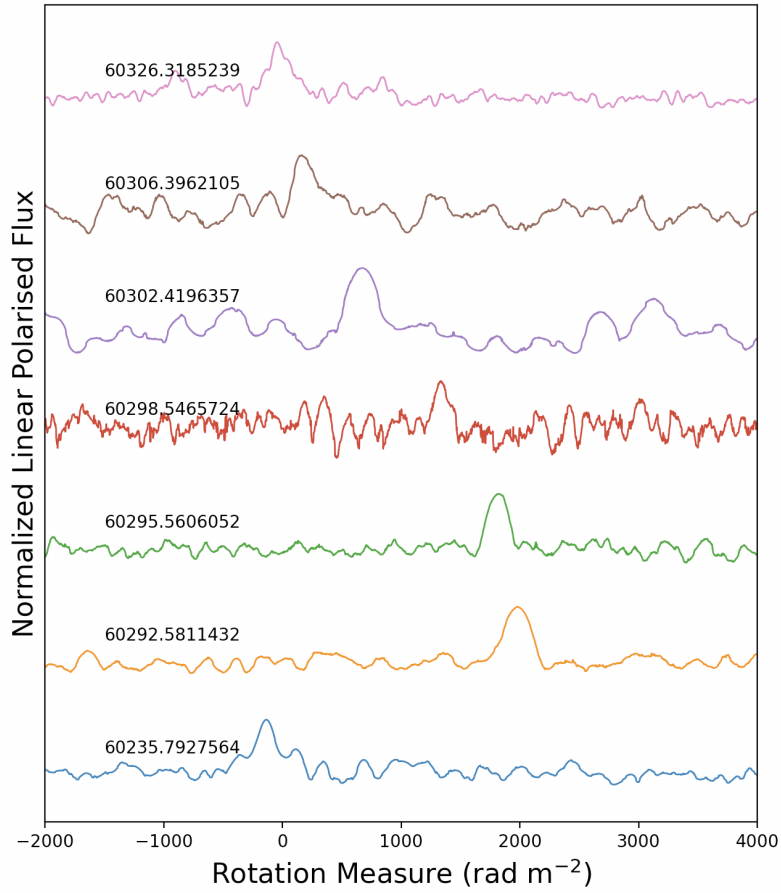


Figure S1: **RM Variability for bursts of FRB 20220529.** The normalized linear polarised flux is shown as a function of RM for seven bursts on different days (sorted by MJDs). The RM of each burst is determined by its maximum linear polarization value.

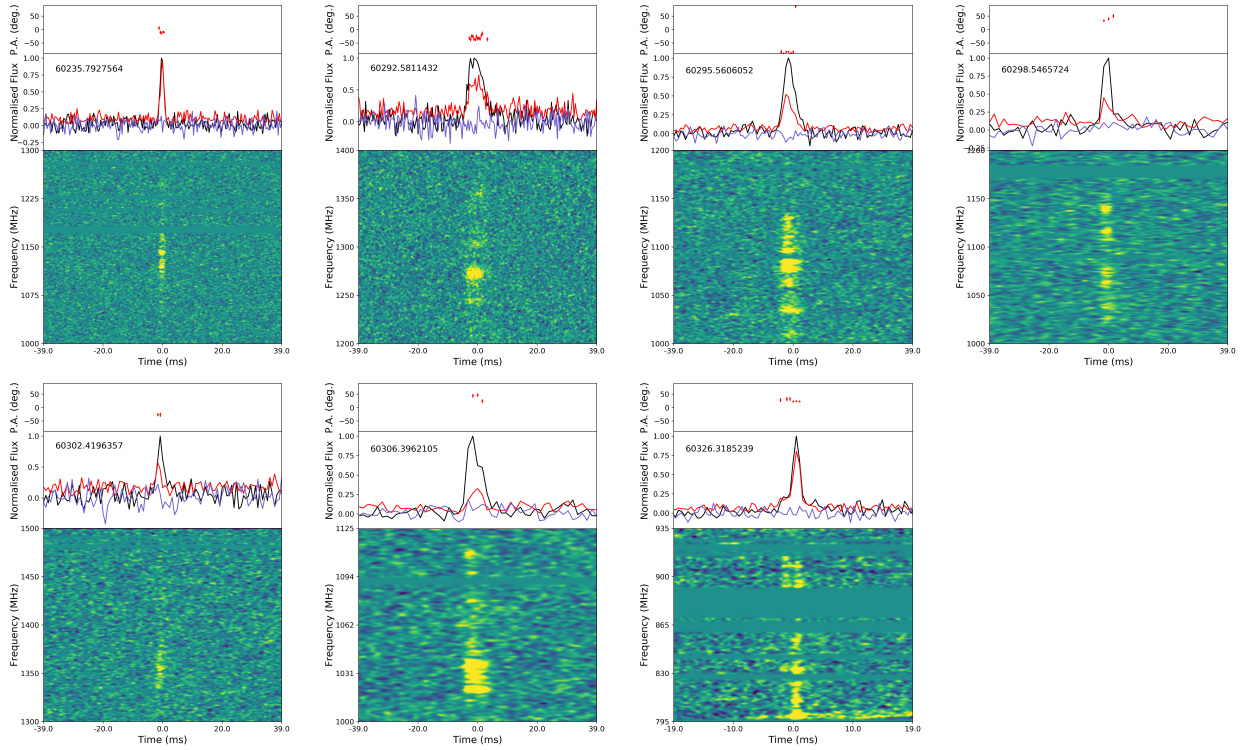


Figure S2: **Polarization profiles of seven bursts on different days from FRB 20220529, ordered by MJDs.** In each subplot, the upper panel displays the position angle of linear polarization at the centre frequency. The middle panel shows the polarization pulse profile, where black, red and blue curves denote total intensity, linear polarization, and circular polarization. The lower panel presents the dynamic spectra for the total intensity for all pulses, with a frequency resolution of 0.97 MHz/channel and time resolution of 393 or 786 μ s/bin.

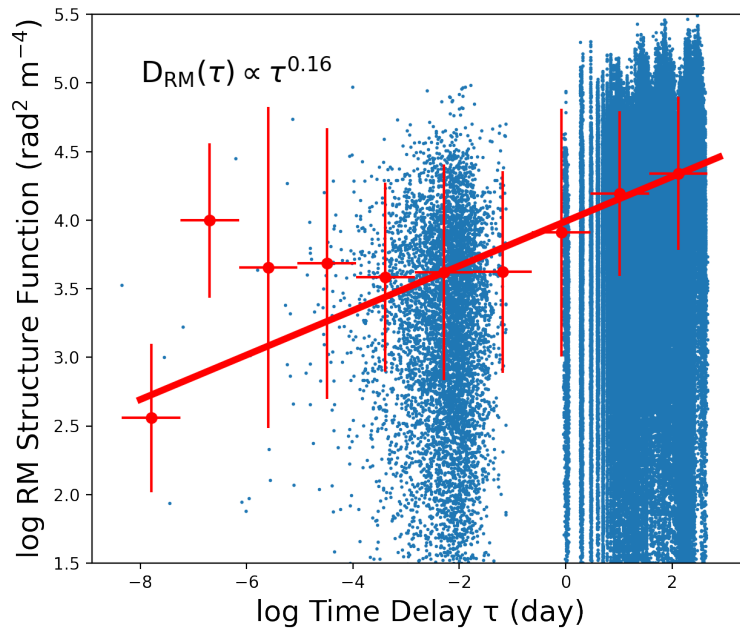


Figure S3: **The structure function of RM.** The best fit result is $D_{\text{RM}}(\tau) \propto \tau^{0.16}$. It is consistent with the large scattering within a day and insignificant variability in long time delay. The index is consistent with those of FRB 121102 and FRB 180916, indicating a supersonic turbulence, in star-forming region or shocked stellar wind in massive stars.

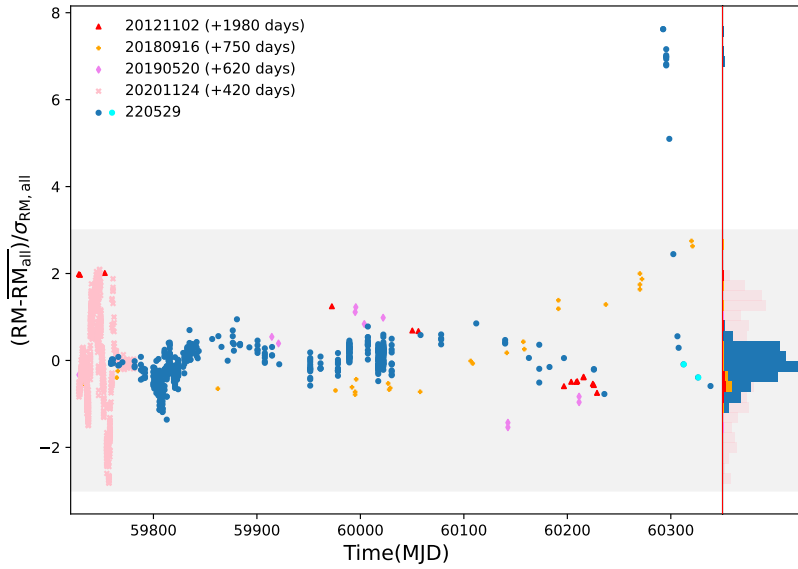


Figure S4: **Significance of RMs for different repeating FRBs.** The significance $(RM - \overline{RM}_{all}) / \sigma_{RM,all}$ of the RMs detected in FRB 20220529 (blue and cyan dots), FRB 20121102 (red triangles) (*13*), FRB 20180916B (*15*) (orange pluses), FRB 20190520B (*14*) (violet diamonds) and FRB 20201124A (*29*) (pink crosses). The $\sigma_{RM,all}$ is the standard deviation of the RM for each FRB. The grey region covers three standard deviations.

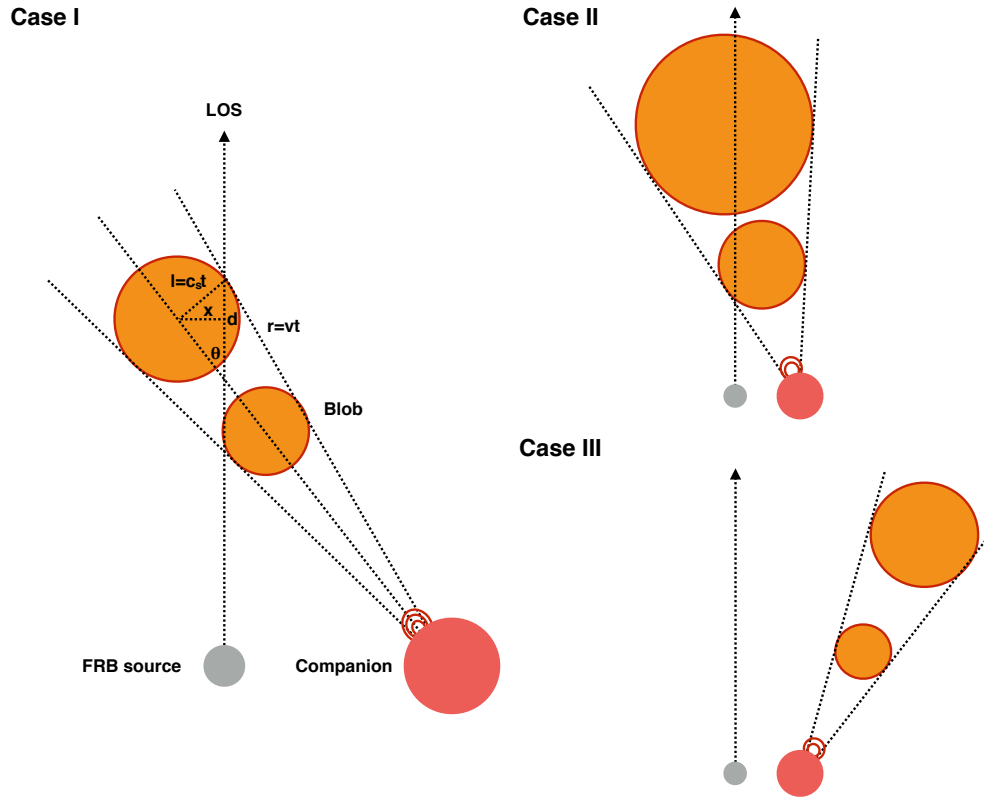


Figure S5: **Schematic configuration of a coronal mass ejection (CME) from a companion star in a binary system.** The grey circle denotes the FRB source, the red circle denotes the companion star, and the orange circles denote an expanding CME. Three cases are discussed in the following discussion. Case I: a CME moves across the line of sight (LOS) in a limited time. Case II: a CME is always on the LOS after a certain time. Case III: a CME does not move on the LOS.

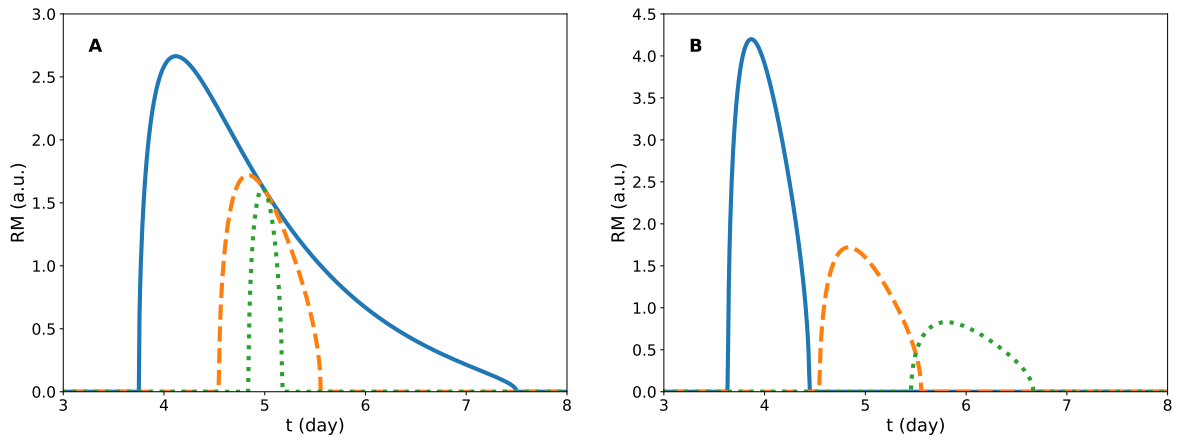


Figure S6: **Predicted RM evolution of a blob from a stellar flare for Case I.** (A) The solid, dashed, and dotted lines correspond to the RM evolution with $t_c = 5$ day and $v \sin \theta / c_s = 3, 10, 30$, respectively. (B) The solid, dashed, and dotted lines correspond to the RM evolution with $v \sin \theta / c_s = 10$ and $t_c = 4, 5, 6$ day, respectively. The phase-zero time corresponds to the explosion time of the stellar flare.

Table S1: **Observation log of FRB 20220529 in FAST and Parkes during the RM flare phase.**

UTC	observational duration seconds	N_{FRB}	R_{FRB} hour ⁻¹
FAST			
2024-01-29	1200	1	3
2024-01-10	1800	0	0
2024-01-04	1800	0	0
2023-12-29	3600	1	1
2023-12-28	1200	4	12
2023-12-24	2400	4	6
2023-12-20	2400	2	3
2023-12-17	3600	15	15
2023-12-14	1200	4	12
2023-11-22	1200	0	0
2023-11-07	1200	0	0
2023-10-18	1200	3	9
Parkes			
2024-01-29	12660	0	0
2024-01-17	8700	1	0.4
2024-01-11	4020	0	0
2024-01-06	6840	0	0
2024-01-05	6420	0	0
2024-01-03	5940	1	0.6
2023-12-22	12000	5	1.5
2023-12-21	9000	1	0.4

Table S2: **Host Candidates**

RA	Dec	m_r	r_{50}	separation	P_{cc}
deg	deg	mag	arcsec	arcsec	
19.10450	20.63269	21.24 ± 0.03	1.17	1.4	0.013
19.10570	20.63302	21.64 ± 0.02	0.30	5.5	0.070
19.10277	20.63320	20.30 ± 0.01	0.48	5.7	0.028
19.10558	20.63399	20.05 ± 0.01	0.63	7.4	0.038